

Dielectric Junction: Electrostatic Design for Charge Carrier Collection in Solar Cells

Jürgen Hüpkes, Uwe Rau, and Thomas Kirchartz*

Conventional solar cells typically use doping of the involved semiconducting layers and work function differences between highly conductive contacts for the electrostatic design and the charge selectivity of the junction. In some halide perovskite solar cells, however, substantial variations in the permittivity of different organic and inorganic semiconducting layers strongly affect the electrostatic potential and thereby indirectly also the carrier concentrations, recombination rates, and eventually efficiencies of the device. Here, numerical simulations are used to study the implications of electrostatics on device performance for classical p–n junctions and p–i–n junctions, and for device geometries as observed in perovskite photovoltaics, where high-permittivity absorber layers are surrounded by low-permittivity and often also low-conductivity charge transport layers. The key principle of device design in materials with sufficiently high mobilities that are still dominated by defect-assisted recombination is the minimization of volume with similar densities of electrons and holes. In classical solar cells this is achieved by doping. For perovskites, the concept of a dielectric junction is proposed by the selection of charge transport layers with adapted permittivity if doping is not sufficient.

1. Introduction

A crucial element ensuring functionality of photovoltaic devices is the existence of charge-selective junctions that ensure preferential extraction of electrons and holes at different contacts and subsequently net current flow at short circuit.^[1–5] While the p–n junction is the prototypical charge-selective junction featured in most introductory texts and courses on photovoltaics, it is by far not the only charge-selective device geometry.^[1,2,6,7] In fact, with

the transition of silicon photovoltaics from diffused junction concepts to silicon heterojunction solar cells,^[8–10] the classical p–n homojunction becomes less relevant for current photovoltaic technologies. Instead, a wide range of device geometries and junction types exist for inorganic and organic solar cells, most of which rely mainly on charge-selective layers of different work functions, which are attached to the actual absorber layer.^[1]


The properties like work functions and doping densities of the different layers of a solar cell not only ensure efficient charge separation but may also have a substantial influence on the recombination rate at different working points and thereby on the solar cell's power conversion efficiency.^[11] Low-mobility absorber materials as used in organic or amorphous silicon solar cells are therefore always implemented in p–i–n-type or metal-insulator-metal-type geometry, where an intrinsic absorber layer is sandwiched between two highly conductive

semiconductors, metals, or metal oxide layers with different work functions. The resulting carrier depletion in the absorber layer results in an electric field extending throughout the absorber layer that improves charge carrier collection. In contrast, for high-mobility semiconductors such as crystalline Si or III/V semiconductors, a large field-free region is beneficial to reduce strong recombination in the narrow depletion region, where electron and hole concentrations are similar. Solar cell geometries could therefore be classified by the extent of the depletion region relative to the total absorber thickness,^[11] and the choice of device geometry would depend mostly on charge carrier mobilities in the absorber layer as well as on technological constraints such as the available doping range of certain materials. In amorphous Si, for instance, doping would lead to high defect densities and short charge carrier lifetimes thereby creating the necessity to keep any doped layers very thin.^[12] In Cu(In, Ga)Se₂, p-type doping would exist without introducing additional dopants but just as a consequence of the existence of intrinsic, charged defects.^[13–15]

So far, all frequently used photovoltaic device geometries use the control over doping densities and work functions to define the electrostatics of the device. With the recent advent of halide perovskite solar cells, however, two additional aspects have become crucial: 1) the existence of charged intrinsic defects that may move inside the device and thereby create time-dependent doping profiles^[16–23] and 2) the combination of (relatively)

J. Hüpkes, U. Rau, T. Kirchartz
IEK5-Photovoltaik
Forschungszentrum Jülich
Wilhelm-Johnen-Str., 52425 Jülich, Germany
E-mail: t.kirchartz@fz-juelich.de

T. Kirchartz
Faculty of Engineering and CENIDE
University of Duisburg-Essen
Carl-Benz-Str. 199, Duisburg 47057, Germany

 The ORCID identification number(s) for the author(s) of this article can be found under <https://doi.org/10.1002/solr.202100720>.

© 2021 The Authors. Solar RRL published by Wiley-VCH GmbH. This is an open access article under the terms of the Creative Commons Attribution License, which permits use, distribution and reproduction in any medium, provided the original work is properly cited.

DOI: 10.1002/solr.202100720

high-mobility^[24–26] and high-permittivity^[27,28] absorber materials combined with low-permittivity and low-conductivity charge transport layers (CTL).^[29]

The present article focuses on the implication of the second observation, that is, the impact that mostly organic CTLs can have on the electrostatics and subsequently on the performance of a solar cell. Especially, in inverted halide perovskite solar cells, undoped organic transport layers such as PTAA as hole transport material and a variety of fullerenes such as C₆₀, PCBM or ICBA are frequently used as electron transport material.^[29–31] Given that the permittivity of lead halide perovskites is fairly high ($\epsilon_r \approx 30$),^[27] while that of organic semiconductors is approximately one order of magnitude smaller ($\epsilon_r \approx 3$),^[32] a substantial part of the built-in voltage of a halide perovskite solar cell will drop over the low-permittivity contact layers.^[29,33] The thickness, permittivity, and conductivity of these layers will thereby affect the electron and hole concentration in the absorber layer and subsequently the recombination rate and the device performance.^[34]

At first, we give a very general introduction to the effect of electrostatics on device performance and present the common doped p–i–n and p–n junctions as examples. We explain the link between electrostatics, electron and hole densities, and subsequently the recombination rate. To reduce the recombination rate under illumination at a given external voltage, we need ideally two things to happen: First, the excess charge carrier density from irradiation at, for example, the maximum power point should be as close as possible to the charge carrier density at the same voltage in the dark. Whether there is a difference between the two mostly depends on the mobility of the different layers and the electric field distribution. The second criterium is that for a given product n_p of electron and hole density, the recombination rate should be minimized. This can be achieved by having a large asymmetry between electron and hole densities. This means that recombination rates can be minimized by slowing down the slower of the two capture processes (i.e., either electron and hole capture by the defect).^[35]

Both of these guiding principles for device design depend on the depth-dependent electrostatic potential, which should be a key design element for efficient solar cells. We highlight that, in addition to the well-known concept of doping, the permittivity affects how the electrostatic potential difference between two contacts will drop over layers with relatively low conductivity. Especially in halide perovskite solar cells, large permittivity variations between absorber and charge transport layers occur and may thereby affect photovoltaic performance. Depending on the mobility, we then arrive at different design principles that can help to better understand performance differences in solar cells and also define directions in designing solar cell layer stacks for high efficiency.

The solar cells are simulated using the device simulator ASA, which solves three coupled differential equations on a 1D grid in a steady-state situation (no variations over time).^[36] These differential equations are the two continuity (drift-diffusion) equations describing the generation, transport, and recombination of electrons and holes as well as the Poisson equation describing the connection between space-charge and electrostatic potential. The equations are solved with appropriate boundary conditions that describe the injection and extraction of electrons and holes

at either contact in case of the continuity equations. In case of the Poisson equation, the work functions of anode and cathode set the boundary conditions for the electrostatic potential. ASA does not include the transport of mobile ions. More details on the modeling approach are provided in Supporting Information.

2. Basic Theory

2.1. Electrostatics and Recombination Rates

The article deals with the overarching question of how electrostatics affects the photovoltaic device performance via its influence on recombination rates. Recombination rates are relevant for all working points of a solar cell. At short circuit, the balance between carrier extraction and recombination determines the efficiency of charge carrier collection. At open circuit, it is likewise the balance between photogeneration and recombination of charge carriers that determines the open-circuit voltage V_{oc} . In most solar cell technologies, there are three relevant recombination mechanisms, namely, radiative recombination, Auger recombination, and Shockley–Read–Hall (SRH) recombination, each of which has a different dependence of the rate of recombination on the concentration of charge carriers. Radiative recombination is always present given that it is the inverse process of photogeneration.^[37,38]

However, for most practical solar cell technologies other than GaAs,^[39,40] radiative recombination is not the dominant recombination mechanism. This is due to the fact that most thin-film solar cell technologies are based on the use of polycrystalline or amorphous layers, where various lattice defects in the bulk, at surfaces and interfaces, or at grain boundaries cause nonradiative recombination to be substantially accelerated relative to the case of a perfect lattice. This acceleration of charge recombination by defects is mathematically described mostly using the Shockley–Read–Hall^[41,42] formalism and is a consequence of the increased probability of phonon-assisted processes in the presence of deep localized states caused by defects.^[43]

In the case of crystalline Si, another important factor is the reduction of radiative recombination as a consequence of the indirect nature of the bandgap.^[44] This leads to the consequence that three-particle Auger processes are substantially more important in Si^[45,46] as compared with direct semiconductors.^[47] Thus, with the exception of GaAs, it is SRH and Auger recombination that have to be minimized by an appropriate choice of the device electrostatics. For Auger recombination, where the recombination rate scales with the square of the majority carrier concentration, this requirement implies to minimize the volume of the absorber that has a very high doping density. This is a well-known fact and is partly responsible for the success of silicon heterojunction concepts relative to diffused emitter geometries, because the amorphous Si layers used to form the p–n junction in the former design feature the high doping density only in a very thin, high-bandgap region of the cell where minority carrier concentrations are extremely small and therefore recombination is of much reduced relevance.^[8,48]

For SRH recombination, the recombination rate has a more complicated dependence on carrier density than for the other two recombination mechanisms, and the consequences are slightly less obvious. The SRH recombination rate can be expressed as

$$R_{\text{SRH}} = \frac{(np - n_i^2)}{(n + n_1)\tau_p + (p + p_1)\tau_n} \quad (1)$$

with electron and hole carrier density n and p , their capture lifetimes τ_n and τ_p , and the equilibrium carrier density n_i . The abbreviations $n_1 = N_C \exp[(E_T - E_C)/kT]$ and $p_1 = N_V \exp[(E_V - E_T)/kT]$ have the unit of a carrier density and become relevant if a trap level E_T is close to either of the band edges (E_C and E_V for conduction and valence band edge, respectively). In this case, the detrapping of charge carriers becomes relevant, while for deep defects, the carrier densities n_1 and p_1 can be neglected relative to either n or p or both.

The most likely scenario for SRH recombination is a relatively deep defect, which dominates the total recombination rate. This is due to the fact that the slower of the two capture processes limits the total rate and that a single transition from one band to a localized state in the gap usually requires the emission of several phonons.^[49,50] For instance, in crystalline Si, a midgap defect would be about 560 meV away from either band. Optical phonon energies are around 58 meV, which implies that ten phonons each would be necessary for both transitions (conduction band to defect and defect to valence band). Given that higher numbers of phonons necessary for a single transition slow down the rate of this transition substantially (in the low-temperature limit, the recombination rate goes approximately with $1/l!$, where l is the number of phonons involved in the transition),^[49,50] shallow defects have a high likelihood that the transition of the opposite band edge is quite slow and hence the whole recombination rate is small. Therefore, the SRH recombination rate is often shown for the case of a deep defect where it simplifies to

$$R_{\text{SRH}} = \frac{(np - n_i^2)}{n\tau_p + p\tau_n} \quad (2)$$

Equation (2) is a crucial equation for understanding the effect of electrostatics and different distributions of $n(x)$ and $p(x)$ as a function of position x . Let us assume for the moment that the cell is at open circuit. Then we know that generation rate and recombination rate integrated up over the volume of the cell must be equal to ensure zero net current flow. This also implies that for a given generation rate, we do not want to minimize the recombination rate (its average value is set by the generation rate), but we want to achieve the highest possible voltage or quasi-Fermi-level (QFL) splitting $\Delta E_f = kT \ln(np/n_i^2)$ for a given generation or recombination rate.^[51] It can be shown mathematically that Equation (2) leads to a maximum value of R_{SRH} for the case $n\tau_p \approx p\tau_n$ (see Supporting Information). Thus, maximizing photovoltaic power conversion efficiency in particular in high-mobility materials requires minimizing the volume where the condition $n\tau_p \approx p\tau_n$ is valid. In practice this means that for high-mobility absorber materials, it is useful to avoid a large volume taken up by a space-charge region.^[52]

The consequence so far is that the optimization criteria may differ depending on whether an electric field is beneficial for charge extraction in low-mobility absorber layers or an electric field is detrimental because it coincides with a large volume where the condition $n\tau_p \approx p\tau_n$ is fulfilled. The latter leads to significant recombination and reduces the photovoltage that is built up at a certain irradiation.

2.2. Efficiency of Classical p–n and p–i–n Junction Solar Cells

There are two classical device geometries that are based on combining semiconductor layers with different doping densities. The first one is the (asymmetric) p–n junction that usually combines one thin highly doped layer (emitter) with one much thicker layer with reduced doping (base), where the terms of emitter and base originate from transistor terminology. The second is the p–i–n junction consisting of a thick intrinsic layer sandwiched between two thin p- and n-type layers. The difference between the two geometries could be summarized by the attempt to minimize (p–n junction) or maximize (p–i–n junction) the volume of the cell that is depleted of charge carriers and therefore has a nonzero electric field. Whether one or the other is more beneficial for photovoltaic performance depends on the mobility lifetime product of the absorber material.

Figure 1 illustrates the difference in photovoltaic efficiency between p–n (black solid) and p–i–n junctions (red dashed) as a function of mobility lifetime product using the parameters shown in Table 1. For both junctions, the efficiency is highly improved by better material quality of the absorber. However, if we compare the efficiency for the same $\mu\tau$ values, two cases are to be distinguished for device-relevant efficiencies. Low-to-moderate $\mu\tau$ values lead to diffusion lengths that are below or of the order of the absorber layer thickness. Here, the p–i–n junction with an extended space-charge region

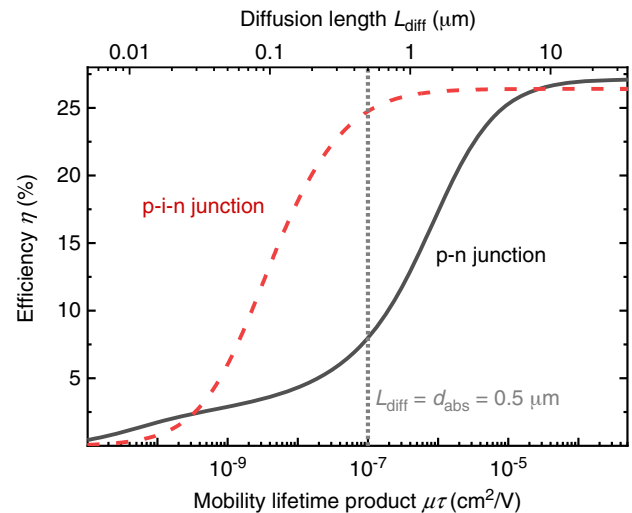


Figure 1. Efficiency η as a function of mobility lifetime product $\mu\tau$ for p–n and p–i–n junctions. Efficiency increases with electronic quality of the absorber. For diffusion lengths of the order of the absorber layer thickness, the electric field in the absorber from the wide space-charge region in the p–i–n device structure enhances the extraction of charge carriers.

Table 1. If not otherwise stated, these parameters have been used for the simulations using ASA. The bold values have been kept constant in all simulations. More details on the device simulation are given in Supporting Information.

Parameter	Symbol	Default values
Active layer thickness	d_{abs}	500 nm
Thickness of CTLs (ETL, HTL)	d_{CTL}	50 nm
Effective density of states conduction/valence band	$N_{\text{CB}}, N_{\text{VB}}$	10^{19} cm^{-3}
Bandgap energy of the absorber	$E_{\text{g,abs}}$	1.6 eV
Bandgap energy of the CTLs	$E_{\text{g,CTL}}$	2.0 eV
Electron/hole mobility in the absorber	$\mu_{n/p,\text{abs}}$	Low: $0.01 \text{ cm}^2 \text{ V}^{-1} \text{ s}^{-1}$ High: $100 \text{ cm}^2 \text{ V}^{-1} \text{ s}^{-1}$
Electron/hole mobility in CTLs	$\mu_{n/p,\text{CTL}}$	$10 \text{ cm}^2 \text{ V}^{-1} \text{ s}^{-1}$
Effective SRH lifetime	$\tau_{n,p}$	1 μs (absorber) 0.1 μs (CTL)
Doping density in doped CTLs	$N_{\text{D}}, N_{\text{A}}$	10^{18} cm^{-3}
Doping density in absorber for doped junctions	$N_{\text{D}}, N_{\text{A}}$	0, 10^{17} cm^{-3}
Relative dielectric permittivity of absorber and CTL	ϵ_r	3, 30, 10^4 (dielectric) 10 (doped junctions)
Auger coefficient in absorber ^[58]	C_{Auger}	$5.4 \times 10^{-28} \text{ cm}^6 \text{ s}^{-1}$

and a significant electric field in the total volume of the absorber yield better performance than the p–n junction. For large diffusion lengths, given by $\mu\tau \geq 10^{-5} \text{ cm}^2 \text{ V}^{-1}$ for an assumed absorber thickness $d_{\text{abs}} = 500 \text{ nm}$, the efficiency is maximized and is not limited anymore by charge carrier collection. Thus, the enhanced recombination in the wide depletion region limits the efficiency in p–i–n junctions. Note that at very low values of $\mu\tau$ the diffusion length gets larger than the drift length of charge carriers,^[11] so the p–n junction is slightly favored for very low $\mu\tau$ values. However, given the overall low efficiency for diffusion lengths $L_{\text{diff}} \lesssim 0.1 d_{\text{abs}}$, this is without technological relevance.

To support these statements, **Figure 2** shows band diagrams, charge carrier densities n and p , and charge carrier recombination rate R_{rec} of (left) p–i–n and (right) p–n junctions with high $\mu\tau$ product at their respective maximum power points. In the p–i–n junction, the depletion zone extends over the entire absorber. This results in an electric field across the bulk with charge carrier densities $n \approx p$ and thus high recombination rates. In contrast, in the p–n junction, the minority carrier density in the bulk is strongly reduced due to p-type doping in the absorber and the depletion zone shrinks to a narrow volume close to the electron contact.

In p–n junction solar cells, the bigger part of the absorber is field free. Thus, in case of low-mobility absorber materials, the electrons and holes are prone to recombination before

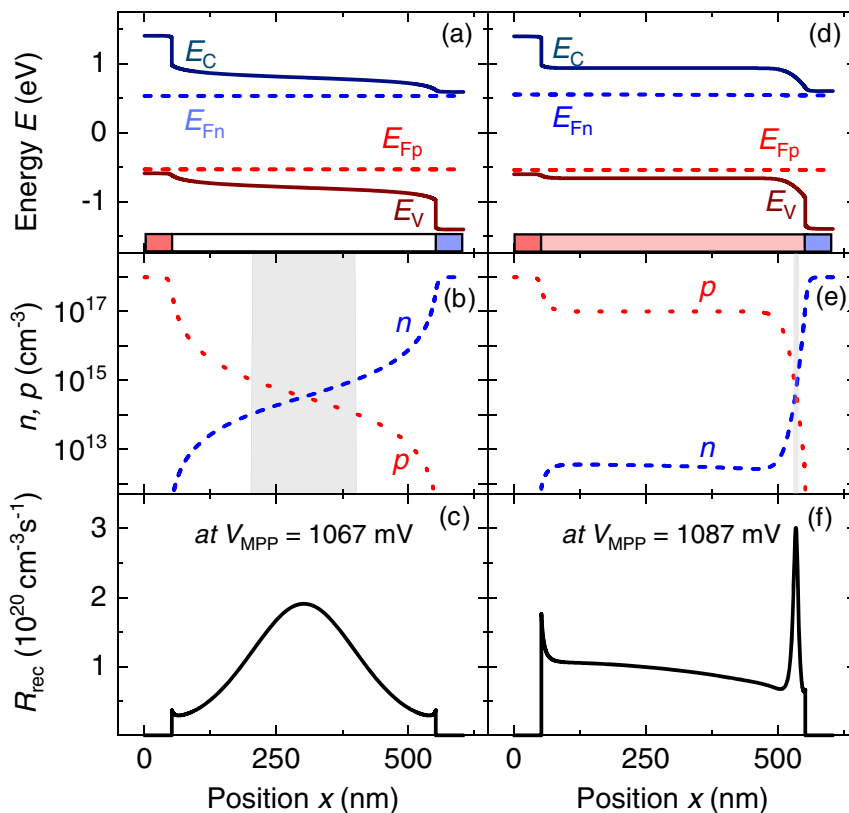


Figure 2. a,d) Band diagrams, b,e) electrons and holes densities n, p , and c,f) recombination rates R_{rec} for doped (a–c) p–i–n and (d–f) p–n junctions. The gray area represents the volume in which $0.1 < \frac{n}{p} < 10$. All data are shown for the respective maximum power point. The mobility lifetime product $\mu\tau$ was set to $10^{-4} \text{ cm}^2 \text{ V}^{-1}$ corresponding to $\mu_{\text{abs}} = 100 \text{ cm}^2 \text{ V}^{-1} \text{ s}^{-1}$. In the p–i–n junction, the space–charge region with an electric field and similar electron and hole density extend over a large absorber volume, while these regions are very narrow in case of the p–n junction.

being extracted. In the former case, the electric field in the absorber of the p–i–n junction supports extraction of charge carriers.

2.3. The Influence of Permittivity Variations on the Electrostatic Potential

In the previous section, we utilized intentional doping for manipulating the charge and electrostatic potential distribution. The electrostatic potential Φ in the solar cell is described by the Poisson equation

$$\Delta\Phi(r) = -\frac{\rho(r)}{\varepsilon(r)} \quad (3)$$

using the charge distribution ρ and the permittivity ε of the involved materials. While in silicon the charge distribution is easily controlled via doping, in other materials effective doping is more difficult.^[53] If we consider hardly any doping, the carrier density distribution is mainly given by the band offsets, generation, recombination, and transport. In a situation where we can neglect any change of charge within this stack (e.g., by a space–charge, by carrier trapping, or accumulation of free carriers due to transport effects), we may use what we denote the “dielectric approximation,” and a solar cell consisting of an absorber material sandwiched between electron and hole transport layers (HTLs) can be considered as a series connection of capacitors with the different layers being the dielectric. That is, we assume that the electrostatic potential V_{tot} across the whole device is shared between the HTL, the absorber (abs), and the electron transport layer (ETL) according to their respective dielectric properties (thickness d and permittivity ε) leading to

$$V_{\text{tot}} = V_{\text{HTL}} + V_{\text{abs}} + V_{\text{ETL}} = \frac{Q}{A} \left(\frac{d_{\text{HTL}}}{\varepsilon_{\text{HTL}}} + \frac{d_{\text{abs}}}{\varepsilon_{\text{abs}}} + \frac{d_{\text{ETL}}}{\varepsilon_{\text{ETL}}} \right) \quad (4)$$

Note that Equation (4) describes how the equilibrium built-in potential difference $V_{\text{bi},0}$ as well as the externally applied voltage V_{ext} is shared between the different layers. Any charge Q/A (per unit area) shows up at the contacts outside the layer stack only, which is a good approximation in particular for situations where the overall charge carrier densities in the absorber and the CTLs are relatively low, that is, at low voltages in the dark. At higher voltages and with irradiation, the concentration of space–charge due to free charge carriers will lead (according to Equation (3)) to band bending that cannot be explained anymore by Equation (4). However, Equation (4) is useful to explain the general idea on how permittivity will affect the drop of electrostatic potential difference over a certain layer.

The combination of different materials in solar cells, for example, organic charge transport materials (relative permittivity $\varepsilon_r = 3$) and halide perovskite absorbers ($\varepsilon_r = 30$), will have a strong influence on electrostatics and efficiency. The low permittivity in lowly conductive CTL implies that a significant fraction of the voltage drop occurs over the contact layers. Thus, the electric field in the absorber is reduced substantially relative to a situation where the CTLs were highly conductive and had high permittivity.

3. Results and Discussion

3.1. Doped Junctions with Asymmetric Carrier Lifetimes

In the theory section we have compared p–i–n and p–n junctions and explained the effect of the mobility lifetime product and the electrostatics on the efficiency. In a second step we investigate the transition from intrinsic to doped absorber materials in conjunction with asymmetric charge carrier lifetimes. **Figure 3** shows the J – V parameters as a function of doping density in the absorber for low (dashed) and high mobility (solid lines) in the absorber. In addition, the effect of asymmetric charge carrier lifetimes for electrons and holes is shown in different colors. In all cases, the efficiency (Figure 3a) drops for very high doping levels ($>10^{17} \text{ cm}^{-3}$) due to Auger recombination, as indicated by the blue region. For intrinsic and lowly doped absorbers with doping levels below 10^{15} cm^{-3} , the depletion zone extends over the absorber and the electric field supports extraction at low charge carrier mobility. Increasing the doping levels reduces the depletion region width and a basically field-free absorber is formed. While for low charge-carrier mobility in the absorber the diffusion length of charge carriers is lower than the thickness of this layer and poor charge extraction through the field-free region limits J_{SC} and efficiency (red area); in solar cells with high mobilities of charge carriers in the absorber, the diffusion length of charge carriers is sufficiently large for all generated carriers to be extracted. In addition, the doped absorbers benefit from low minority-carrier densities leading to low SRH recombination rates and an increase in fill factor (FF), V_{OC} , and efficiency with moderate doping level. In contrast, for lowly doped (intrinsic) absorbers a large volume of the absorber possesses large densities of electrons and holes at the same time (see Figure 2a), so their recombination via defects is very effective and competes with extraction. Here, FF , V_{OC} , and thus efficiency are reduced.

The asymmetry in charge carrier lifetimes slightly reduced the efficiency level and shifts the optimum doping density. Here, we recall the condition for highest recombination activity, resulting in higher SRH recombination: $n\tau_p = p\tau_n$. The corresponding optimum for high efficiency requires minimizing the volume, which fulfils this condition, while in all other positions either $n\tau_p \gg p\tau_n$ or $n\tau_p \ll p\tau_n$ should be realized. If the absorber is doped with the carrier type of lower lifetime, the product on one side of the inequation gets extremely large. At the same time, the other side of the equation stays constant in high-injection conditions (low doping) or is even reduced at low injection (high doping). In this situation, recombination is suppressed.

This relation can easily be understood if we consider defect-assisted recombination as a two-step capture process of both charge carrier types into the defect.^[35,43] The slower of the two capture processes into a defect state determines the recombination rate. A higher lifetime corresponds to lower capture coefficients and slower capture rates. Thus, doping with the opposite carrier type of lower lifetime reduces the density of the respective recombination partner, and the overall recombination rate is reduced.

3.2. The Concept of Dielectric Junctions

In the previous section, we have demonstrated the interplay between electrostatics, carrier density, and efficiency based on

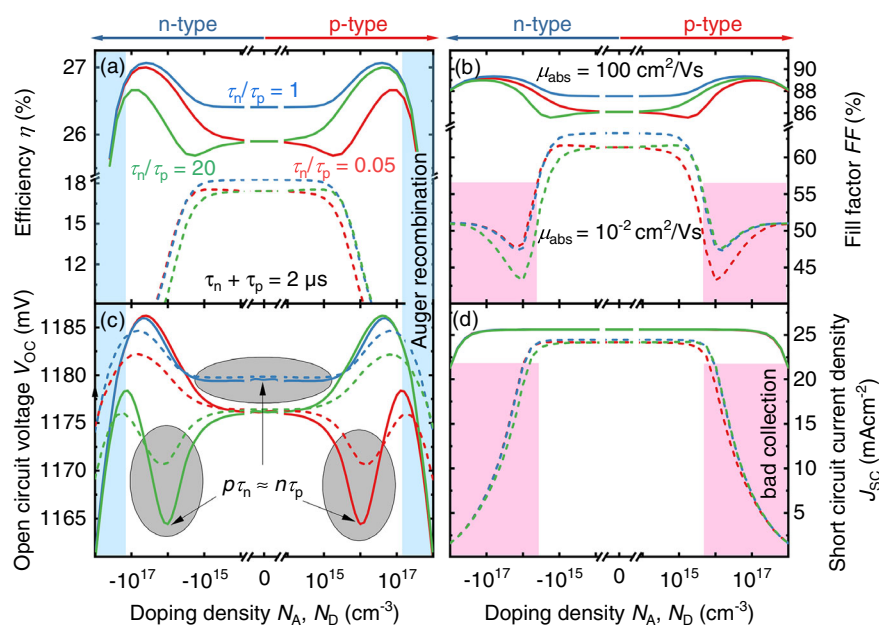


Figure 3. a) Efficiency η , b) FF , c) open-circuit voltage V_{OC} , and d) short-circuit current density J_{SC} of simulated solar cells as a function of their doping density in the absorber for high- (solid lines) and low (dashed lines)-mobility μ in the 500 nm-thick absorber. The color code represents different charge carrier lifetime ratios for electrons τ_n and holes τ_p , while the arithmetic average of lifetimes was kept constant at $\tau = (\tau_n + \tau_p)/2 = 1\mu s$. An intrinsic absorber is favorable for low mobility in the absorber, while for high-quality absorbers, doped absorbers outperform the p–i–n junction. The lifetime asymmetry causes a lower efficiency level and slightly shifts the optimum doping density. The red and blue areas represent conditions with low charge carrier collection efficiency and strong Auger recombination, respectively.

variable doping density within the absorber combined with doped contact layers. As given by Equation (4), the voltage drop in the different layers is also controlled by different values of the permittivity in the solar cell's layer stack. **Figure 4** shows band diagrams for undoped junctions under illumination at short circuit. The position-dependent electric field F_E is given by the local gradient of the bands divided by the elementary charge

$$F_E = \frac{\nabla E_{C/V}}{q} \quad (5)$$

We distinguish four different cases that are inspired by halide perovskite solar cells. Figure 4a represents an undoped junction with all layers having the same permittivity. Thus, the electric field spreads equally over all layers (**case A**). If we replace the CTLs by low-permittivity materials, for example, organic materials, the field in the absorber is reduced as shown in Figure 4b (**case B**). To extend this situation to a completely field-free absorber, we further assume ionic screening in the halide perovskite absorber (**case C**). According to the previous discussions, the resulting cell would require high charge carrier mobilities and lifetimes for good charge extraction. Here, ionic screening is emulated by introducing very high permittivity in the absorber. Similar to screening of moving ions, high permittivity causes the electric field in the absorber to vanish. A comparison of the dielectric approximation of ionic screening using a high-permittivity material with the presence of mobile ions in normal-permittivity materials is provided in (Figure S5, Supporting Information). The discussed situations in this context are well

represented by the dielectric approximation. In case C, the absorber represents a field-free region with the electric field symmetrically extending solely over both CTLs. As a result, the QFLs are equally spaced from their respective bands. From this, we deduce roughly equal densities for electrons and holes $n \approx p$ in a wide volume in the absorber. The situation drastically changes if we replace one of the CTLs, for example, the HTL, by a high-permittivity material (see Figure 4d, **case D**). The field solely remains in the electron contact, while the absorber and the HTL remain field free. Thus, both quasi-Fermi levels in the absorber shift downward with respect to the bands. As a consequence, the QFL for holes is much closer to the valence band than in case of symmetric electrostatics as observed in case C, so in the absorber the concentration of electrons is much lower than the one of holes $n \ll p$, which is in favor of lower recombination rates.

Another effect influencing the electric field distribution in the solar cell is the resistive loss from charge carrier transport.^[35,54] In lead halide perovskite absorber layers, the mobilities of electrons and holes are sufficiently high to ignore resistive transport losses in the absorber.^[55] However, some organic contact layers suffer from low conductivity.^[56,57] **Figure 5** shows the J – V parameters of the solar cells from Figure 2 and 4 for a variation of the charge carrier mobility in the CTLs. Here, all mobilities in ETLs and HTLs for electrons and holes are considered equally. In all cases, the efficiency increases continuously with charge carrier mobility in the CTLs, while it saturates beyond $0.1\text{ cm}^2\text{ V}^{-1}\text{ s}^{-1}$. The corresponding efficiency level is determined by the cell design and parameters like charge carrier

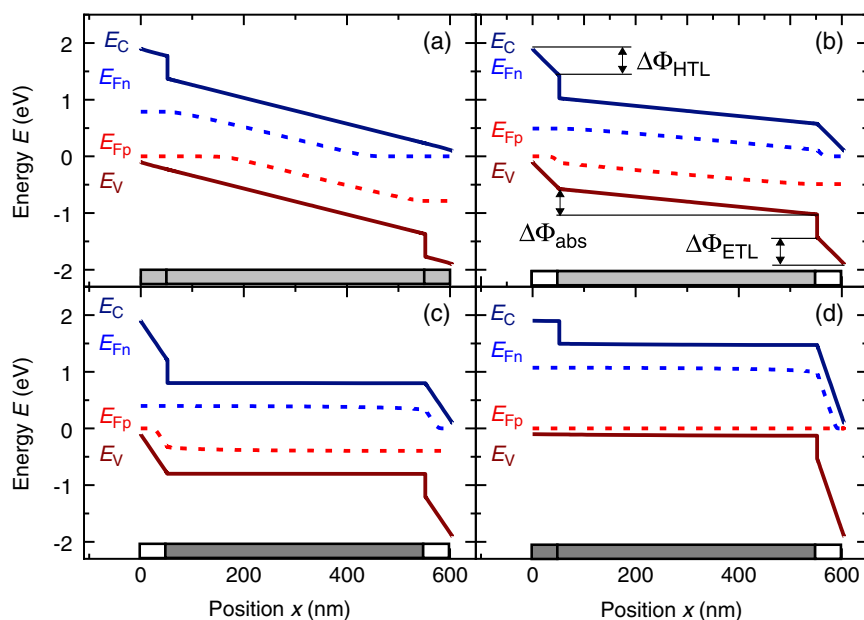


Figure 4. Band diagrams of DJs at short circuit for halide perovskite solar cells with a relative absorber permittivity of $\epsilon_{r,abs} = 30$: a) case A) junction with equal permittivity in all layers; b) case B) organic contact layers ($\epsilon_{r,abs} = 3$) without and c) case C) with ionic screening in the absorber; d) case D) high-permittivity hole contact and ionic screening in the absorber. The ionic screening is included by high absorber permittivity ($\epsilon_{r,abs} = 10000$). The bars at the bottom of each graph indicate the device stack with the layer's relative permittivity given by the brightness of the color (bright for low and dark for high permittivity, respectively). The DJs A, B, and C represent symmetric device architectures with decreasing electric field in the absorber and symmetric charge carrier distribution. Case D represents a field-free region in the absorber with asymmetric field in the CTLs and downward shift of both quasi-Fermi levels leading to $p \gg n$. The electrostatic potential differences $\Delta\Phi$ for the CTLs and the absorber are defined exemplarily in (b).

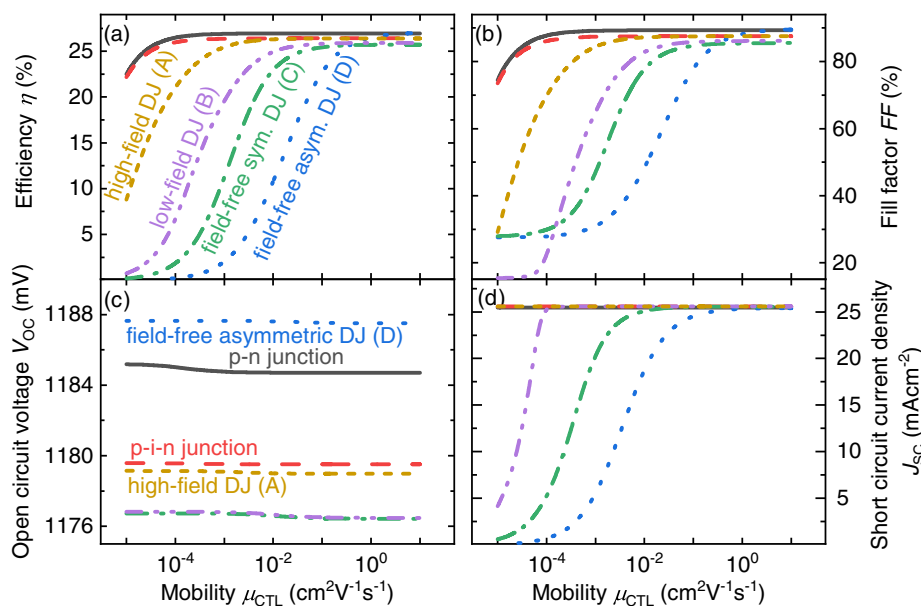


Figure 5. a) Efficiency η , b) FF , c) open-circuit voltage V_{OC} , and d) short-circuit current density J_{SC} of simulated solar cells as a function of mobility in electron and HTLs for various junction designs. Efficiency increases in all cases, while the sensitivity to μ_{CTL} and the maximum efficiency level are defined by the type of junction. All absorbers offer high charge carrier mobilities of $100 \text{ cm}^2 \text{ V}^{-1} \text{ s}^{-1}$.

mobility in the absorber (see Figure S2, Supporting Information), which determine losses from charge recombination, charge carrier collection, and transport. The doped

junctions with their doped CTLs do not suffer from low mobility in the CTLs because their conductivity remains rather high. In the DJs, the CTLs are undoped. Here, their conductivity is

determined by the charge injection from the absorber. For low mobilities in the CTLs, FF and J_{SC} break down. However, this effect is counteracted if charge extraction is supported by a significant electric field in the absorber of the DJ.

As discussed before, the electric field and the resulting electrostatic potential difference $\Delta\Phi$ in the absorber can be an important parameter for the efficiency.^[54] In **Figure 6** we plot the JV parameters of DJs as a function of the relative electrostatic potential difference in the absorber for high-mobility absorbers and various charge carrier mobilities in the CTLs for the solar cells of cases A–D and the transition between these distinct cases. For this, we have gradually changed the material permittivities of CTLs and/or absorber. The symmetric devices (equal properties of HTLs and ETLs in cases A, B, C) show consistently increasing efficiency with the electrostatic potential difference in the absorber. This trend is independent of conductivity in the CTLs, though the absolute values follow the dependencies given in **Figure 5**. However, for the asymmetric case D, the electrostatic potential difference is not relevant and the device is very sensitive to CTL conductivity. For low mobilities in the CTLs, the asymmetric case shows much lower performance than all symmetric devices, though the electric field is still much higher than that in case C. This is governed by poor extraction as seen by the low FF and J_{SC} . If resistive losses in the CTLs can be neglected, the asymmetric device even outperforms the symmetric device with a high electric field in the absorber due to the higher voltage. The situation for low-mobility absorber materials is presented in **Figure S3**, Supporting Information.

To clarify the situation in DJs, **Figure 7** exhibits the band diagrams and charge carrier density distribution in the four specific cases of **Figure 4** with high mobility in the CTLs at their respective maximum power point. Case A with electron and hole

contact having the same permittivity as the absorber offers similar electrostatics as the p–i–n-type cell without absorber doping (see **Figure 2a**). The electric field is rather uniformly distributed over the volume and the electron and hole density increases and decreases rather exponentially in the absorber, respectively. Here, high electron and hole concentrations, which correspond to high recombination rates, are observed around the center of the absorber. The gray area highlights the volume, in which the electron and hole concentrations differ by less than a factor of ten. Case B was inspired by halide perovskite solar cells with organic CTLs. This case is a transition to case C with additional screening of electric field in the absorber. The electric field in the absorber is reduced and the voltage drop is shifted to the contact layers by their lower permittivity. Thus, the electron and hole concentrations are similar throughout nearly the whole absorber (gray area) but at a slightly lower value than in case A. The resulting recombination spreads over the absorber volume. If we replace the organic HTL by a high-permittivity HTL in case D, the absorber becomes highly p-type (without any doping!) and the junction volume is strongly decreased like in a p–n-type doped junction (see **Figure 2b**). Note that in case D, n and p always differ by more than a factor of 100, so here the gray area is completely gone. Similar to the doped p–n junction, recombination is suppressed by the very low minority carrier density, resulting in the best-performing device with high V_{OC} , if not lowly conductive CTLs, or absorbers governing the charge distribution and limiting device performance.

Figure 8 shows the JV parameters of DJs of cases A–D and of the doped junctions from **Figure 1** as a function of the mobility lifetime product in the absorber. The graph clearly distinguishes cells, where charge carrier collection is primarily driven either by an electric field in the bulk of the absorber or by diffusion with a

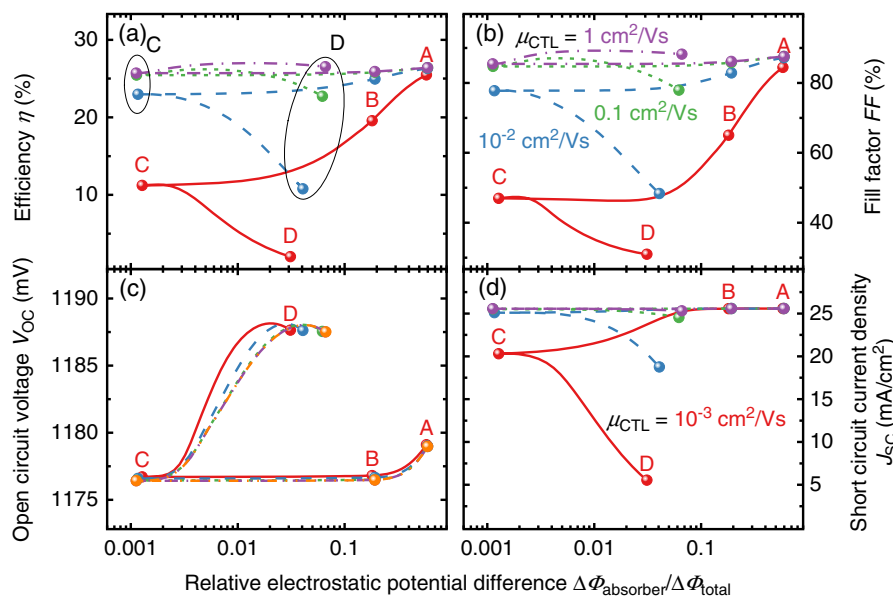


Figure 6. a) Efficiency η , b) FF , c) open-circuit voltage V_{OC} , and d) short-circuit current density J_{SC} of simulated solar cells as a function of the electrostatic potential difference $\Delta\Phi_{abs}$ in the absorber relative to the total electrostatic potential difference in the whole cell $\Delta\Phi_{total}$ at the respective maximum power point. The data represent the DJs from **Figure 5** with additionally stepwise varied permittivities to show the gradual transition from case A via B and C to D. The color code represents different levels of μ_{CTL} , which are given as labels in the graph. All absorbers offer high charge carrier mobilities of $100 \text{ cm}^2 \text{ V}^{-1} \text{ s}^{-1}$.

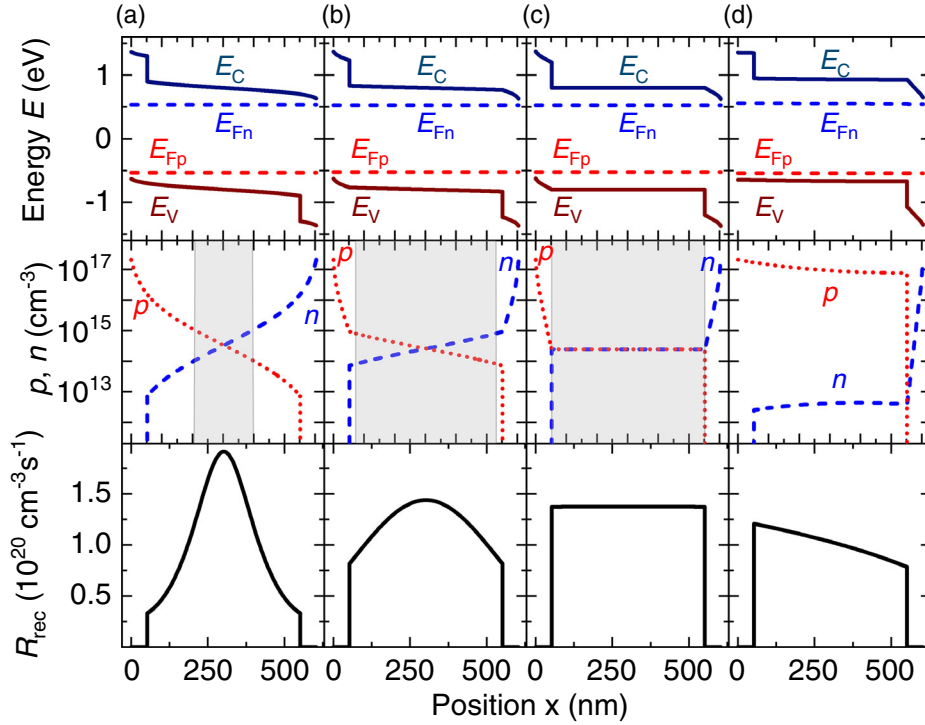


Figure 7. Band diagrams, electron and hole densities n and p , and recombination rates R_{rec} for the different DJs introduced in Figure 4: a) case A, b) case B, c), case C, and d) case D. The gray area represents the volume in which n and p are similar ($0.1 < \frac{n}{p} < 10$). All values were evaluated at the individual maximum power point. The mobility lifetime product $\mu\tau$ was set to $10^{-4} \text{ cm}^2 \text{ V}^{-1}$ corresponding to $\mu_{\text{abs}} = 100 \text{ cm}^2 \text{ V}^{-1} \text{ s}^{-1}$. The symmetric junctions A, B, and C represent transition from high-field to low-field absorbers with a wide region of similar electron and hole densities. Case D, in contrast, is a device where in the absorber holes are in excess of electrons. Simulations using SETFOS for similar junctions in the dielectric approximation or with mobile ions are provided in Figure S4 and S5, Supporting Information.

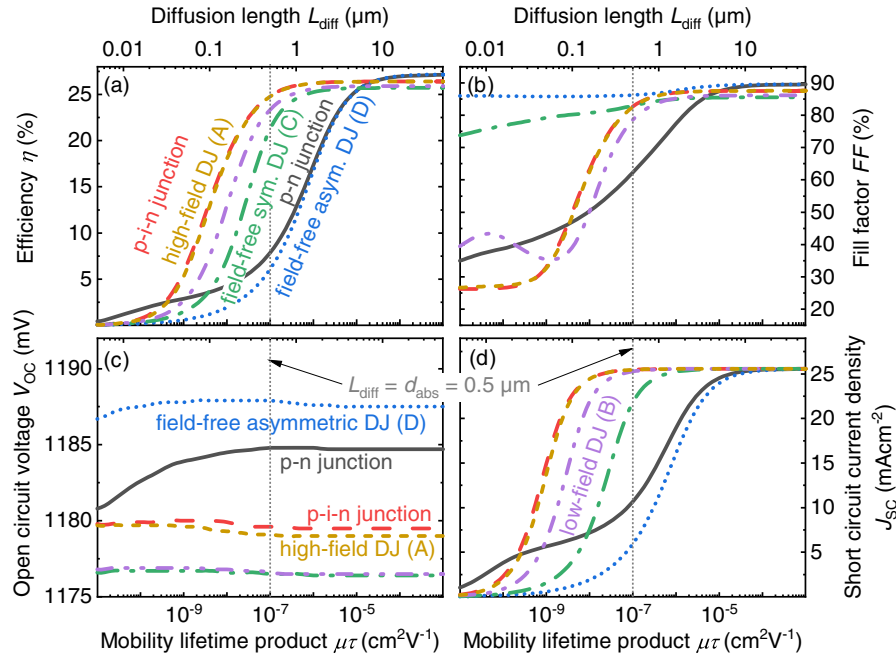


Figure 8. a) Efficiency η , b) FF , c) open-circuit voltage V_{OC} , and d) short-circuit current density J_{SC} of simulated solar cells as function of mobility lifetime $\mu\tau$ product for different doped and DJs. For diffusion lengths of the order of the absorber layer thickness, an electric field in the absorber supports the extraction of charge carriers.

very narrow space—charge region. The symmetric DJs A, B, and C generally behave like the doped p–i–n cell with still good charge carrier collection at diffusion lengths of the order of the absorber layer thickness. In contrast, the asymmetric DJ with the field-free region roughly follows the trend of the doped p–n junction. The short-circuit current density of the DJ D drops much faster than the one of the p–n junction for low diffusion length, while the *FF* stays rather high.

In conclusion, DJs without any doping can be designed by the choice of materials with appropriate permittivity similarly as doped junctions. Depending on the electronic quality of the materials (e.g., charge carrier mobility and lifetime), symmetric junctions with an electric field extending over the absorber or asymmetric junctions with a wide field-free region are favorable. For high-quality absorber materials like halide perovskites with high charge carrier mobilities, a symmetric device architecture should be avoided. Instead, asymmetry in CTLs is favored, which means, that permittivity and/or thickness of ETL and HTL should be different.

4. Conclusion

We have introduced the concept of a DJ. Such a junction is achieved by stacking of the HTL, the absorber, and the ETL with largely different permittivities between two electrodes of different electron affinities. In such a device, the electrostatics is controlled solely by the permittivities of the individual layers and the work function difference of the electrodes but doping of the semiconducting layers making up the solar cell is not of relevance. However, we have shown that DJs can be designed in ways that show a behavior and performance very similar to doped junctions.

In contrast to doped junctions, where the electrostatic design and charge distribution are determined by doping of CTLs and the absorber, in DJs, the field distribution and charge carrier densities are determined by the interplay between the thickness and permittivity of all layers in the device. In addition, charge separation via drift or diffusion is counteracted if the extraction is limited by low mobilities in the undoped contact layers.

Depending on the conductivity of the CTLs and the mobility lifetime product in the absorber, the electrostatics should be designed in a different way. We discussed four distinct cases: strong field-assisted charge separation (case A and B) with different levels of electric fields in the absorber as observed in p–i–n-type solar cells and a field-free region absorber with a narrow junction volume with either equidistant quasi-Fermi levels to their respective bands (case C) and asymmetric quasi-Fermi levels (case D) like in a p–n junction with p-doped absorber.

While charge separation should be driven by an electric field in the absorber for low-mobility CTLs or low-quality absorber materials, for high-quality absorbers in conjunction with highly mobile charges in the CTLs, a narrow junction volume suppresses recombination. The latter one is achieved by an asymmetric device design using CTLs of different permittivities in combination with a field-free (high-permittivity) absorber material.

Supporting Information

Supporting Information is available from the Wiley Online Library or from the author.

Acknowledgement

The authors acknowledge the Helmholtz Association for funding via the PEROSEED project.

Open access funding enabled and organized by Projekt DEAL.

Conflict of Interest

The authors declare no conflict of interest.

Data Availability Statement

The data that support the findings of this study are available from the corresponding author upon reasonable request.

Keywords

doping, electric fields, halide perovskites, permittivity, recombination

Received: September 6, 2021

Revised: October 30, 2021

Published online: November 16, 2021

- [1] P. Würfel, *Physics of Solar Cells: From Basic Principles to Advanced Concepts*, Wiley VCH, Weinheim, Germany **2009**.
- [2] U. Würfel, A. Cuevas, P. Würfel, *IEEE J. Photovoltaics* **2015**, 5, 461.
- [3] R. Brendel, R. Peibst, *IEEE J. Photovoltaics* **2016**, 6, 1413.
- [4] E. T. Roe, K. E. Egelhofer, M. C. Lonergan, *ACS Appl. Energy Mater.* **2018**, 1, 1037.
- [5] U. Rau, T. Kirchartz, *Adv. Mater. Interfaces* **2019**, 6, 1900252.
- [6] U. Rau, G. Kron, J. H. Werner, *J. Phys. Chem. B* **2003**, 107, 13547.
- [7] T. Kirchartz, U. Rau, *Introduction to Thin-Film Photovoltaics*, Wiley-VCH Verlag GmbH & Co. KGaA, Weinheim, Germany **2011**, p. 1.
- [8] K. Yoshikawa, H. Kawasaki, W. Yoshida, T. Irie, K. Konishi, K. Nakano, T. Uto, D. Adachi, M. Kanematsu, H. Uzu, K. Yamamoto, *Nat. Energy* **2017**, 2, 17032.
- [9] K. Yoshikawa, W. Yoshida, T. Irie, H. Kawasaki, K. Konishi, H. Ishibashi, T. Asatani, D. Adachi, M. Kanematsu, H. Uzu, K. Yamamoto, *Sol. Energy Mater. Sol. Cells* **2017**, 173, 37.
- [10] S. De Wolf, A. Descoedres, Z. C. Holman, C. Ballif, *Green* **2012**, 2, 7.
- [11] T. Kirchartz, J. Bisquet, I. Mora-Sero, G. Garcia-Belmonte, *Phys. Chem. Chem. Phys.* **2015**, 17, 4007.
- [12] R. E. I. Schropp, M. Zeman, *Amorphous and Microcrystalline Silicon Solar Cells: Modeling, Materials and Device Technology*, Springer, Boston, MA **1998**, p. 207.
- [13] S. B. Zhang, S.-H. Wei, A. Zunger, H. Katayama-Yoshida, *Phys. Rev. B* **1998**, 57, 9642.
- [14] H.-W. Schock, R. Noufi, *Prog. Photovoltaics: Res. Appl.* **2000**, 8, 151.
- [15] J. Bekaert, R. Saniz, B. Partoens, D. Lamoen, *Phys. Chem. Chem. Phys.* **2014**, 16, 22299.
- [16] N. Tessler, Y. Vaynzof, *ACS Energy Lett.* **2020**, 5, 1260.
- [17] N. E. Courtier, J. M. Cave, J. M. Foster, A. B. Walker, G. Richardson, *Energy Environ. Sci.* **2019**, 12, 396.

- [18] R. A. Belisle, W. H. Nguyen, A. R. Bowring, P. Calado, X. Li, S. J. C. Irvine, M. D. McGehee, P. R. F. Barnes, B. C. O'Regan, *Energy Environ. Sci.* **2017**, 10, 192.
- [19] P. Calado, A. M. Telford, D. Bryant, X. Li, J. Nelson, B. C. O'Regan, P. R. F. Barnes, *Nat. Commun.* **2016**, 7, 13831.
- [20] E. T. Hoke, D. J. Slotcavage, E. R. Dohner, A. R. Bowring, H. I. Karunadasa, M. D. McGehee, *Chem. Sci.* **2015**, 6, 613.
- [21] Z. Xiao, Y. Yuan, Y. Shao, Q. Wang, Q. Dong, C. Bi, P. Sharma, A. Gruverman, J. Huang, *Nat. Mater.* **2015**, 14, 193.
- [22] A. Crovetto, M. K. Huss-Hansen, O. Hansen, *Sol. Energy* **2017**, 149, 145.
- [23] L. Bertoluzzi, C. C. Boyd, N. Rolston, J. Xu, R. Prasanna, B. C. O'Regan, M. D. McGehee, *Joule* **2020**, 4, 109.
- [24] L. M. Herz, *ACS Energy Lett.* **2017**, 2, 1539.
- [25] C. Motta, F. El-Mellouhi, S. Sanvito, *Sci. Rep.* **2015**, 5, 12746.
- [26] T. M. Brenner, D. A. Egger, A. M. Rappe, L. Kronik, G. Hodes, D. Cahen, *J. Phys. Chem. Lett.* **2015**, 6, 4754.
- [27] M. Sendner, P. K. Nayak, D. A. Egger, S. Beck, C. Müller, B. Epding, W. Kowalsky, L. Kronik, H. J. Snaith, A. Pucci, R. Lovrincic, *Mater. Horiz.* **2016**, 3, 613.
- [28] J. N. Wilson, J. M. Frost, S. K. Wallace, A. Walsh, *APL Mater.* **2019**, 7, 010901.
- [29] O. J. Sandberg, J. Kurpiers, M. Stolterfoht, D. Neher, P. Meredith, S. Shoaee, A. Armin, *Advanced Materials Interfaces* **2020**, 7, 2000041.
- [30] Z. Liu, J. Siekmann, B. Klingebiel, U. Rau, T. Kirchartz, *Adv. Mater.* **2021**, 11, 2003386.
- [31] K. A. Bush, C. D. Bailie, Y. Chen, A. R. Bowring, W. Wang, W. Ma, T. Leijtens, F. Moghadam, M. D. McGehee, *Adv. Mater.* **2016**, 28, 3937.
- [32] S. Torabi, F. Jahani, I. Van Severen, C. Kanimozhi, S. Patil, R. W. A. Havenith, R. C. Chiechi, L. Lutsen, D. J. M. Vanderzande, T. J. Cleij, J. C. Hummelen, L. J. A. Koster, *Adv. Funct. Mater.* **2015**, 25, 150.
- [33] S. Wheeler, D. Bryant, J. Troughton, T. Kirchartz, T. Watson, J. Nelson, J. R. Durrant, *J. Phys. Chem. C* **2017**, 121, 13496.
- [34] M. Stolterfoht, V. M. Le Corre, M. Feuerstein, P. Caprioglio, L. J. A. Koster, D. Neher, *ACS Energy Lett.* **2019**, 2887.
- [35] B. Das, Z. Liu, I. Aguilera, U. Rau, T. Kirchartz, *Mater. Adv.* **2021**, 2, 3655.
- [36] M. Zeman, J. van den Heuvel, B. E. Pieters, M. Kroon, J. Willemen, *Advanced Semiconductor Analysis*, TU Delft, The Netherlands **2003**.
- [37] W. van Roosbroeck, W. Shockley, *Phys. Rev.* **1954**, 94, 1558.
- [38] T. Kirchartz, U. Rau, *Phys. Status Solidi A* **2008**, 205, 2737.
- [39] M. A. Green, A. W. Y. Ho-Baillie, *ACS Energy Lett.* **2019**, 4, 1639.
- [40] J. F. Guillemoles, T. Kirchartz, D. Cahen, U. Rau, *Nat. Photonics* **2019**, 13, 501.
- [41] W. Shockley, W. T. Read, *Phys. Rev.* **1952**, 87, 835.
- [42] R. N. Hall, *Phys. Rev.* **1952**, 87, 387.
- [43] B. Das, I. Aguilera, U. Rau, T. Kirchartz, *Phys. Rev. Mater.* **2020**, 4, 024602.
- [44] T. Trupke, M. A. Green, P. Würfel, P. P. Altermatt, A. Wang, J. Zhao, R. Corkish, *J. Appl. Phys.* **2003**, 94, 4930.
- [45] A. Richter, M. Hermle, S. W. Glunz, *IEEE J. Photovoltaics* **2013**, 3, 1184.
- [46] A. Richter, S. W. Glunz, F. Werner, J. Schmidt, A. Cuevas, *Phys. Rev. B* **2012**, 86, 165202.
- [47] T. Kirchartz, L. Krückemeier, E. L. Unger, *APL Mater.* **2018**, 6, 100702.
- [48] A. Augusto, J. Karas, P. Balaji, S. G. Bowden, R. R. King, *J. Mater. Chem. A* **2020**, 8, 16599.
- [49] B. K. Ridley, *Solid-State Electron.* **1978**, 21, 1319.
- [50] B. K. Ridley, *J. Phys. C: Solid State Phys.* **1978**, 11, 2323.
- [51] R. Brendel, H. J. Queisser, *Sol. Energy Mater. Sol. Cells* **1993**, 29, 397.
- [52] M. J. Stocks, A. Cuevas, A. W. Blakers, *Prog. Photovoltaics: Res. Appl.* **1996**, 4, 35.
- [53] A. Walsh, A. Zunger, *Nat. Mater.* **2017**, 16, 964.
- [54] C. Ahläng, M. Nyman, R. Österbacka, *Phys. Rev. Appl.* **2021**, 16, 014041.
- [55] S. H. Turren-Cruz, M. Saliba, M. T. Mayer, H. Juarez-Santiesteban, X. Mathew, L. Nienhaus, W. Tress, M. P. Erodici, M. J. Sher, M. G. Bawendi, M. Gratzel, A. Abate, A. Hagfeldt, J. P. Correa-Baena, *Energy Environ. Sci.* **2018**, 11, 78.
- [56] P.-W. Liang, C.-C. Chueh, S. T. Williams, A. K. Y. Jen, *Adv. Mater.* **2015**, 5, 1402321.
- [57] W.-J. Chi, P.-P. Sun, Z.-S. Li, *Phys. Chem. Chem. Phys.* **2016**, 18, 27073.
- [58] I. L. Braly, D. W. deQuilettes, L. M. Pazos-Outón, S. Burke, M. E. Ziffer, D. S. Ginger, H. W. Hillhouse, *Nat. Photonics* **2018**, 12, 355.